Operando X-ray scattering and pH tracking reveal a four stage crystallization pathway during calcium carbonate precipitation

Alain Gibaud,[1,2] Özgür Gülmez,[3] Sandy Auguste,[1]

Basab Chattopadhay,[4] Rodrigo Sanches Pires,[5]
Seniz Ucar[3,6] and Yuriy Chushkin,[5]

July 1, 2026

[1] IMMM, UMR 6283 CNRS, Le Mans Université, 72085 Le Mans, France
[2] SWUST, Sichuan, Mianyang, Fucheng District, 621010, China
[3] Department of Metallurgical and Materials Engineering, Middle East Technical University, 06800 Ankara, Turkiye
[4] Department of Physics, Norwegian University of Science and Technology, Høgskoleringen 5, Trondheim 7491, Norway
[5] ESRF - The European synchrotron, 71 avenue des Martyrs, , 38000 Grenoble, France
[6] Department of Chemical Engineering, Norwegian University of Science and Technology, Høgskoleringen 5, Trondheim 7491, Norway

Supplementary Information

S.I. 1: SAXS analysis

The SAXS analysis was performed using a custom MATLAB-based program (*SAXS-analysis*) developed by A. Gibaud [1]. The objective was to describe the scattering evolution during the aggregation and crystallization of calcium carbonate while accounting simultaneously for the particle form factor $P(q,t)$ and the structure factor $S(q,t)$.

Immediately after mixing the two precursor solutions, the experimental SAXS profiles could not be reproduced using a single particle population and instead required a bimodal particle size distribution, consistent with recent observations

reported by Khurts [2]. The normalized form factor of a monodisperse spherical particle of radius r is given by

$$P(q,r) = \left[\frac{3\left(\sin(qr) - qr\cos(qr)\right)}{(qr)^3}\right]^2. \tag{1}$$

For polydisperse particles, the scattering contribution is averaged over a Gaussian radius distribution $g_i(r)$,

$$F_i(q) = \int_{R_{\min}}^{R_{\max}} V_i(r)^2 P_i(q,r)\, g_i(r)\, \mathrm{d}r, \tag{2}$$

where $V_i(r)$ is the particle volume. For a bimodal distribution, the total form-factor contribution becomes

$$F(q) = \frac{f\, F_1(q)}{V_{\text{eff},1}} + \frac{(1-f)\, F_2(q)}{V_{\text{eff},2}}, \tag{3}$$

with

$$V_{\text{eff}} = \frac{\langle V^2 \rangle}{\langle V \rangle},$$

and f the volume fraction of the first population.

The measured SAXS intensity is written as

$$I(q) = K \frac{Q_P}{2\pi^2} F(q)\, S(q), \tag{4}$$

where K is a scale factor and Q_P is the Porod invariant.

For non-interacting particles, $S(q) = 1$. Although this approximation is approximately valid immediately after mixing ($t \approx 0$ s), the scattering rapidly evolves toward strongly correlated regimes that cannot be described by independent particle populations. This requires a non-trivial structure factor capable of capturing (i) low-q amplification, (ii) intermediate-q depletion, and (iii) convergence toward unity at large q.

Classical descriptions such as Percus–Yevick hard-sphere theory or fractal aggregation models ([3, 4, 5] do not reproduce this combination of features, particularly the simultaneous low-q enhancement and intermediate-q dip observed in the fluctuation-dominated regime. We therefore adopt an empirical representation using three Ornstein–Zernike-type contributions [6]:

$$S(q) = 1 + \left[\sum_{i=1}^{3} \frac{A_i}{\left(1 + (q/q_i)^2\right)^D}\right] \exp\left[-(q/q_{\text{cut}})^4\right]. \tag{5}$$

This formulation reproduces the experimentally observed features while ensuring $S(q) \to 1$ at large q. In practice, the first and third terms are positive, while the second term is negative to account for the transient depletion at intermediate q. The exponent D is fixed to 1. The validity of this approach is illustrated in Fig. 1.S1, which shows the decomposition into $F(q)$, $S(q)$ and the

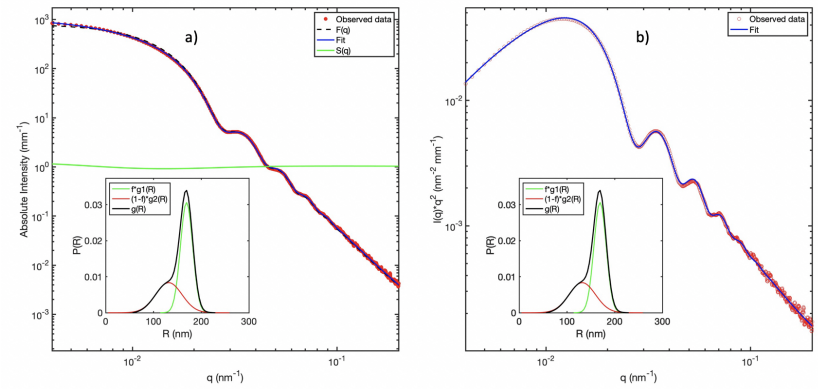

Figure 1.S1: (a) Measured (red dots) and calculated (blue line) intensities at $t = 2$ s, showing contributions of form factor (black dashed) and structure factor (green). (b) Kratky representation highlighting agreement across the full q range.

total intensity $I(q)$, together with the corresponding size distributions. Note that $S(q)$ is fairly flat so that the intensity is mainly described by the form factor (dashed line in the plot of Fig1:S1a)).

The same procedure was applied at different times to track the coupled evolution of structure and interparticle interactions during the transformation (Fig. 2.S1). The different panels explicitly show that $S(q)$ evolves strongly over time, whereas the form factor remains comparatively unchanged. This contrast highlights that the transformation is primarily governed by the development of interparticle correlations rather than significant modifications of the primary particle size distribution except at t=51s where the ACC fringes disappear.

To further justify the use of three contributions in the empirical structure factor, we express $S(q)$ as the Fourier transform of the density–density correlation function,

$$S(q) = \langle \rho(\mathbf{q})\rho(-\mathbf{q}) \rangle. \tag{6}$$

Decomposing the total electron density into amorphous and crystalline contributions,

$$\rho(\mathbf{q}) = \rho_{\mathrm{ACC}}(\mathbf{q}) + \rho_{\mathrm{crystal}}(\mathbf{q}),$$

leads to

$$S(q) = S_{\mathrm{ACC}}(q) + S_{\mathrm{crystal}}(q) + S_{\mathrm{ACC-crystal}}(q), \tag{7}$$

where the cross-correlation term is given by

$$S_{\mathrm{ACC-crystal}}(q) = 2\,\mathrm{Re}\,\langle \rho_{\mathrm{ACC}}(\mathbf{q})\rho_{\mathrm{crystal}}(-\mathbf{q}) \rangle\,. \tag{8}$$

This term captures spatial correlations between density fluctuations in the amorphous calcium carbonate (ACC) network and the emerging crystalline domains, and is non-zero whenever the two populations are not statistically independent.

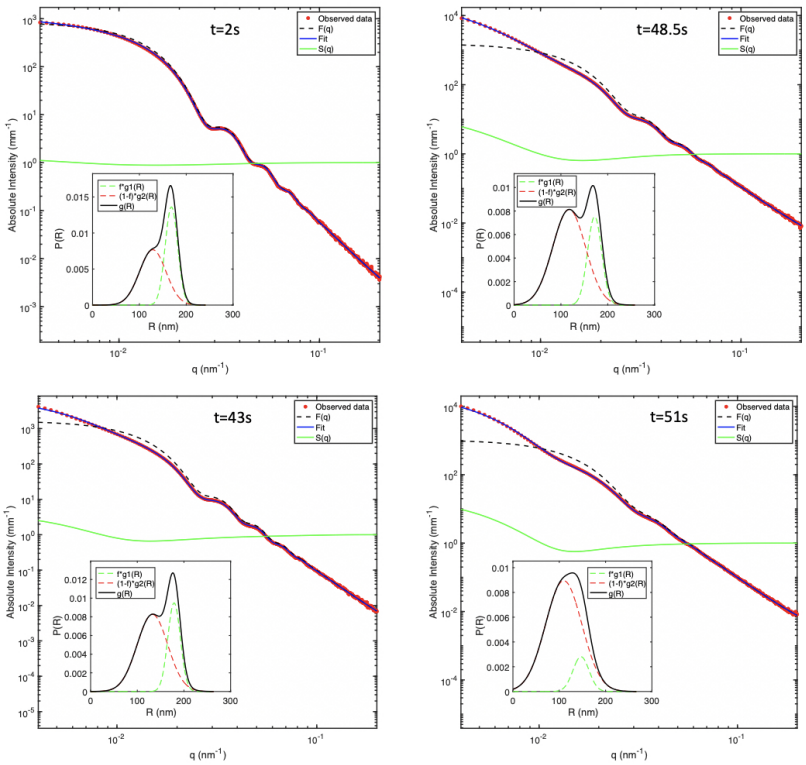

Figure 2.S1: The measured (red dots) and calculated (blue line) scattering intensities for the sample stirred at 250 rpm are presented at selected times (t = 2 s, 43 s, 48.5 s, and 53 s, corresponding to stages I to III). The figure emphasizes the contributions of the different components involved in the modeling. A steady increase in the structure factor ($S(q)$) (green curve) is observed, while the form factor (black dashed line) remains largely unchanged. The inset shows the evolution of the particle size distribution, revealing a clear shift toward smaller radii over time.

Importantly, the experimental system does not allow these contributions to be separated into independent scattering populations. Instead, crystallization develops within a pre-existing correlated ACC fluctuation field, implying that $S_{\mathrm{cross}}(q)$ is non-zero and strongly time-dependent.

In practice, we do not model S_{ACC}, S_{crystal}, and S_{cross} separately. Rather, we use an effective representation that captures their combined effect. The empirical structure factor can therefore be interpreted as a coarse-grained approximation of these three coupled contributions:

$$S(q) = S_{\mathrm{eff}}(q) \simeq S_{\mathrm{ACC}}(q) + S_{\mathrm{crystal}}(q) + S_{\mathrm{cross}}(q). \tag{9}$$

Within this interpretation, each term of the sum can be viewed as a coarse-grained representation of different contributions to the total correlation field: (i) long-wavelength ACC-dominated fluctuations, (ii) intermediate-scale depletion associated with structural reorganization and cross-coupling, and (iii) short-range recovery toward uncorrelated scattering at high q.

The necessity of three terms therefore reflects the fact that the measured $S(q)$ is not a simple particle-particle correlation function, but the Fourier-space signature of a mixed ACC–crystal fluctuation field with non-negligible cross-correlations.

This interpretation is further supported by the failure of incoherent superposition models,

$$I(q,t) = I_{\mathrm{ACC}}(q,t) + I_{\mathrm{crystal}}(q,t), \tag{10}$$

which neglect $S_{\mathrm{cross}}(q)$ and cannot reproduce the low-q amplification, the intermediate-q dip, or the persistence of the Kratky peak.

An alternative description is obtained by expressing the total scattering in terms of coherent amplitudes,

$$I(q,t) = |A_{\mathrm{ACC}}(q,t) + A_{\mathrm{crystal}}(q,t)|^2, \tag{11}$$

which naturally generates an interference contribution,

$$I(q,t) = |A_{\mathrm{ACC}}|^2 + |A_{\mathrm{crystal}}|^2 + 2\,\mathrm{Re}\left[A_{\mathrm{ACC}} A^*_{\mathrm{crystal}}\right]. \tag{12}$$

This formulation is formally consistent with the structure-factor decomposition, since both approaches describe scattering arising from correlated fluctuations between amorphous and crystalline domains rather than from independent particle populations. In the density-correlation formalism, these couplings are contained in the cross term $S_{\mathrm{ACC-crystal}}(q)$, whereas in the amplitude formalism they appear as interference contributions between A_{ACC} and A_{crystal}.

At first sight, the two descriptions therefore appear conceptually similar. However, they differ fundamentally in their physical interpretation. In the coherent two-phase description, the total intensity is constructed from two distinct scattering amplitudes, A_{ACC} and A_{crystal}, each associated with its own form factor and electron-density contrast. The interference term therefore describes explicit correlations between two structurally distinct scattering populations.

Such an approach implicitly assumes that the amorphous and crystalline domains can already be identified as separate entities.

In contrast, the present SAXS analysis employs a single effective form factor $F(q)$ associated primarily with the ACC nanoparticle population, while the evolving mesoscale correlations are incorporated through an effective structure factor $S(q)$. Within this framework, the low-q amplification and transient Kratky peak are interpreted as collective density correlations developing inside a dynamically restructuring fluctuation field rather than as the independent scattering contribution of a separate crystalline particle population.

This distinction is important because the experimental SAXS data do not support the presence of two fully independent scattering populations. In particular, the characteristic Kratky maximum appears before the disappearance of the ACC form-factor oscillations and remains at nearly the same position even after crystalline Bragg peaks become detectable by WAXS. Moreover, attempts to reproduce the SAXS evolution using explicit superpositions of large crystalline particles and residual ACC particles systematically fail to capture both the low-q behaviour and the transient dip observed in $S(q)$. Importantly, $S(q)$ already deviates significantly from unity during phase I and up to the middle of phase II, that is, well before any Bragg reflections are detectable, demonstrating that strong interparticle correlations develop prior to the onset of detectable crystallinity.

A direct comparison between both descriptions is shown in Fig. 3.S1 at $t = 47.5$ s, where ACC begins to coexist with emerging crystalline peaks in the WAXS data. A mixed model combining ACC scattering measured at $t = 40$ s with crystalline scattering measured at $t = 53.5$ s, together with an explicit interference contribution, reproduces the main features of the experimental data. However, a consistently better agreement is obtained using the effective $S(q)$ formulation. This comparison remains necessarily approximate because the crystalline contribution evolves continuously during the transformation and cannot be rigorously represented by a single later-time measurement.

Although the coherent superposition formalism provides a rigorous conceptual framework, its quantitative implementation would require knowledge of the relative phase factor entering the interference term,

$$2\sqrt{I_{\mathrm{ACC}} I_{\mathrm{crystal}}}\cos\phi(q),$$

which is experimentally inaccessible in the present operando SAXS measurements. In the comparison shown in Fig. 3.S1, this phase contribution was approximated by assuming maximal constructive interference. In addition, the continuously evolving and spatially heterogeneous nature of the ACC–crystal transformation makes the definition of a unique phase relation physically ambiguous. The effective structure-factor description adopted here therefore provides a more robust and physically meaningful representation of the collective density fluctuations and cross-correlations governing the transformation.

Importantly, both approaches converge to the same physical conclusion: the ACC and crystalline components are strongly coupled over a narrow transforma-

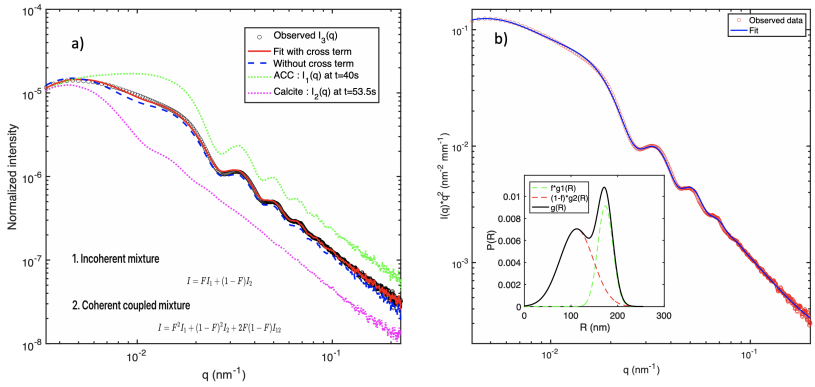

Figure 3.S1: A comparison of the two models : a) using a cross term between the two intensities of ACC and crystal structures and b) the use of S(q).

tion window ($t \approx 47$–52.5 s), during which they cannot be treated as independent scattering populations.

The persistence of the Kratky maximum, stabilizing near

$$q \approx 0.00435 \text{ nm}^{-1},$$

indicates that the dominant length scale is inherited from pre-existing mesoscale correlations within the ACC network, rather than emerging from independent crystalline particle growth.

The appearance of weak Bragg reflections prior to the disappearance of the ACC SAXS signature further confirms that crystallization begins locally within an existing amorphous scaffold. This apparent coexistence is natural because SAXS and WAXS probe distinct length scales: WAXS is sensitive to short-range atomic order, while SAXS reflects mesoscale density fluctuations. Consequently, nanocrystalline domains can already produce detectable Bragg peaks while remaining embedded in an ACC-dominated scattering matrix, contributing weakly to SAXS but strongly to WAXS.

Overall, the data support a coupled fluctuation–ordering mechanism in which crystalline domains emerge within a dynamically correlated ACC network rather than through the independent nucleation and growth of a separate phase.

For a stirring rate of 1000 rpm, the experimental and calculated scattering patterns are shown in Fig. 4.S1. The analysis reveals a strong shift toward smaller characteristic sizes, with two populations centered at 106 ± 36 nm and 167 ± 126 nm at $t = 2$ s. The pronounced dominance of the smaller population (93% volume fraction) indicates that high shear conditions favor the rapid formation of nanoscale building units while strongly suppressing the development of larger aggregates at early times.

This interpretation is further supported by the behavior of $S(q)$, which clearly deviates from unity even at $t = 2$ s. These observations are consistent with a

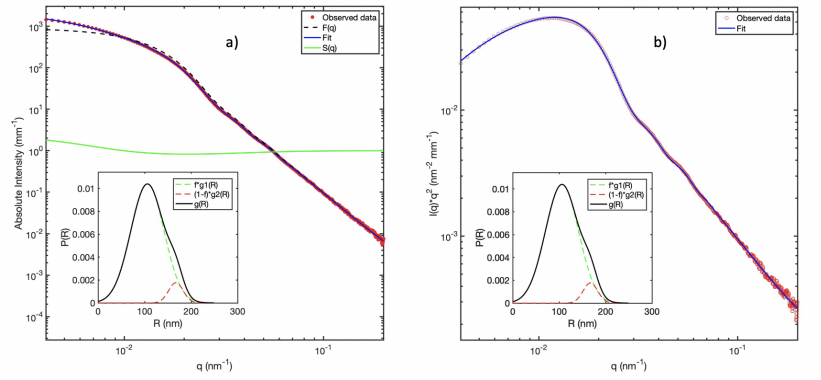

Figure 4.S1: Observed (red dots) and calculated (blue line) scattering intensities of the sample stirred at 1000 rpm at $t = 2$ s. b) Corresponding Kratky representation.

non-classical nucleation pathway in which particle formation proceeds through aggregation-mediated processes rather than through the emergence of a single critical nucleus. The results therefore highlight the key role of hydrodynamic forcing in directing early-stage pathway selection under strongly non-equilibrium conditions.

Overall, the SAXS analysis shows that the structural evolution cannot be interpreted in terms of independent amorphous and crystalline particle populations. Instead, the system evolves as a single correlated density field in which ACC fluctuations and emerging crystalline order are intrinsically coupled.

In principle, an alternative description based on coherent scattering amplitudes,

$$A(q,t) = A_{\mathrm{ACC}}(q,t) + A_{\mathrm{crystal}}(q,t),$$

is formally equivalent to introducing interference terms between distinct scattering contributions. However, this decomposition implicitly assumes that the two components correspond to well-defined, separately identifiable scattering objects with independent form factors. This assumption becomes questionable in the present system, where crystalline domains emerge continuously within a structurally evolving ACC matrix, and where neither phase can be uniquely isolated at intermediate times.

In such a non-stationary and strongly heterogeneous medium, the separation into distinct amplitudes is not uniquely defined and becomes representation-dependent, since the partitioning between "ACC" and "crystal" contributions depends on an arbitrary choice of reference states. As a consequence, the interpretation of the cross term as a fixed physical interaction between two pre-existing populations is not strictly justified.

By contrast, the structure-factor formulation,

$$S(q,t) = \langle \rho(\mathbf{q},t)\rho(-\mathbf{q},t)\rangle,$$

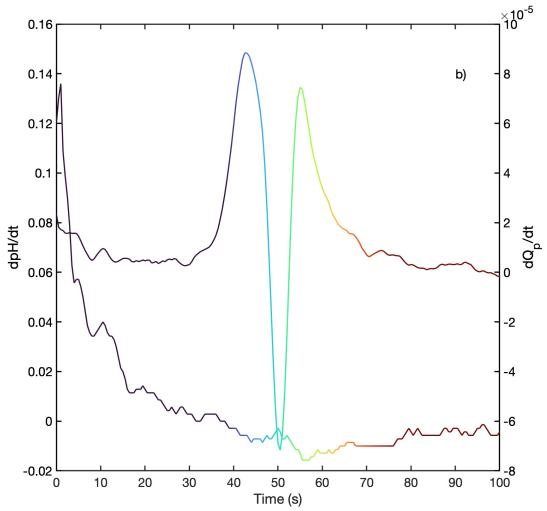

Figure 1.S2: Combined plots showing the derivatives of the pH and of Q_P as a function of time.

remains well-defined as a direct measure of instantaneous density–density correlations, independent of any decomposition into constituent species. The empirical form of $S(q)$ therefore provides a more robust and physically transparent description of the evolving correlated medium.

Within this framework, the persistence of a well-defined mesoscale length scale and the early emergence of crystalline order within a still-dominant ACC scattering background are naturally interpreted as signatures of a fluctuation–ordering mechanism, in which crystallization develops within a pre-correlated amorphous network rather than through independent nucleation and growth of separate particles.

S.I.2: Derivatives of pH and Q_P

We report here the time derivatives of the pH and Q_P inn Fig. Fig. 1.S2. These plots are of particular interest to evidence the rapidity at which the pH and Q_p evolve in the different stages of the process and are discussed in the main text.

S.I. 3: Forward scattering

To gain deeper insight into the evolution of the system during stages I and II, we analyze the forward scattering intensity $I(0)$ together with the structure factor $S(q)$. The results are presented in Fig. 1.S3, where the evolution of the Porod invariant and the effective volume are shown in parallel, with $I(0)$ reported in

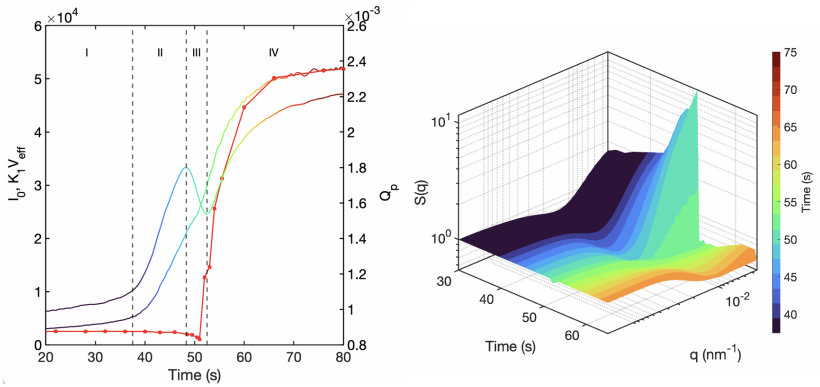

Figure 1.S3: Left panel: time evolution of the Porod invariant Q_P, the forward intensity $I(0)$ measured at the lowest accessible wave vector ($q = 0.0035\,\mathrm{nm}^{-1}$), and the effective volume V_{eff}. Dashed lines indicate the different stages. Right panel: 3D representation of the evolution of the structure factor up to stage IV. The increase in $S(0)$ is accompanied by the development of a dip at intermediate q, which progressively shifts toward higher q during stages II and III. Note that $S(0)$ abruptly collapses at $t \sim 52$ s, indicating a clear departure from classical spinodal decomposition. The colorbar indicates the time scale.

the left panel and $S(q)$ in the right panel.

We observe a continuous increase of the forward scattering throughout the process, while Q_P exhibits a pronounced dip during stage III. This behavior is accompanied by a marked enhancement of $S(q)$ at low wave vectors ($q = 0.0035\,\mathrm{nm}^{-1}$) together with a depletion at intermediate wave vectors ($q = 0.015\,\mathrm{nm}^{-1}$). Such a redistribution of scattering intensity reflects a progressive reorganization of the system across length scales.

At early times, $S(q)$ reflects a well-defined particulate regime characterized by multiple structural features associated with stable ACC particles. As the system evolves, the low-q scattering intensity $S(q \to 0)$ increases markedly, while the intermediate-q minimum becomes progressively more pronounced and shifts toward higher wave vectors. This evolution indicates a redistribution of density fluctuations across length scales accompanied by a reduction in particle size.

By definition, the structure factor is related to fluctuations of the order parameter through

$$S(\mathbf{q}) = \int d\mathbf{r}\, e^{-i\mathbf{q}\cdot\mathbf{r}} \langle \delta\phi(0)\, \delta\phi(\mathbf{r}) \rangle, \tag{13}$$

where $\delta\phi(\mathbf{r})$ denotes local fluctuations of the volume fraction relative to the average composition. Under the assumption of translational invariance, $S(q)$ therefore represents the Fourier transform of the two-point spatial correlation function.

Within equilibrium statistical mechanics, concentration fluctuations are governed by the curvature of the free-energy functional $G(\phi)$. For small fluctuations around a homogeneous state, a quadratic expansion gives

$$S(q) = \frac{k_B T}{\delta^2 G / \delta\phi_q \, \delta\phi_{-q}}. \tag{14}$$

In the long-wavelength limit ($q \to 0$), this reduces to the thermodynamic compressibility relation

$$S(0) \propto \left(\frac{\partial^2 G}{\partial \phi^2} \right)^{-1}_{T,P}, \tag{15}$$

showing that the zero-angle structure factor directly probes the inverse curvature of the free-energy landscape associated with concentration fluctuations. Low-q modes are therefore particularly sensitive to large-scale instabilities and mesoscale reorganization.

Experimentally, the scattering intensity can be expressed as

$$I(q,t) \propto \phi(t)\, V_{\text{eff}}(t)\, P(q)\, S(q,t), \tag{16}$$

where $\phi(t)$ is the average volume fraction, $V_{\text{eff}}(t)$ is the effective scattering volume, $P(q)$ is the particle form factor, and $S(q,t)$ describes collective correlations.

In this representation, the forward scattering and the Porod invariant scale as

$$I(0,t) \propto \phi(t)\, V_{\text{eff}}(t)\, S(0,t), \qquad Q_P(t) \propto \langle (\delta\phi)^2 \rangle, \tag{17}$$

providing complementary measures of the amplitude and spatial distribution of concentration fluctuations.

Comparison of these quantities across the different dynamical regimes reveals a non-trivial redistribution of scattering contributions.

In stage I, $I(0)$, Q_P, and $S(0)$ evolve coherently, consistent with a stable particulate regime characterized by a well-defined length scale and an approximately constant V_{eff}. The Ca^{2+} activity (Supplementary Information S5) remains nearly constant during this stage, indicating that the ACC nanoparticles form a stable colloidal suspension.

In stage II, the system departs from the simple scaling behavior observed at earlier times. While $I(0)$ continues to increase, V_{eff} decreases slightly, indicating a reduction in the effective scattering volume. The increase in forward scattering is therefore dominated by enhanced low-q fluctuations rather than by an increase in particle content. This interpretation is supported by the small decrease in both the Ca^{2+} activity and the pH (Supplementary Information S5). Together with the appearance of weak calcite Bragg peaks during this stage (Figure S4), these observations indicate that crystallization likely initiates at the surface of the ACC network rather than within individual ACC particles. This mechanism explains the strong increase in forward scattering and in $S(0)$ while the characteristic ACC form-factor oscillations remain largely unchanged.

In stage III, a clear decoupling between the different scattering observables emerges. While $I(0)$ and $S(0)$ initially remain high, the Porod invariant Q_P

decreases significantly and the characteristic ACC form-factor oscillations progressively vanish, indicating collapse of the correlated amorphous network. Because V_{eff} decreases only modestly, the dominant structural evolution cannot be attributed simply to particle shrinkage. Instead, the data indicate progressive disappearance of the amorphous fluctuation field as crystalline domains grow at the expense of the ACC phase. During this period, both the Ca^{2+} activity and the pH remain nearly constant, consistent with a rapid and nearly direct transfer of material from the metastable ACC network toward the growing crystalline phase.

The increase in $I(0)$ despite the slight reduction in V_{eff} demonstrates that the scattering evolution is dominated by amplification of long-wavelength concentration fluctuations captured by the increase in $S(0)$. Simultaneously, the structure factor develops a pronounced intermediate-q dip, indicating the emergence of transient mesoscale correlations within an interconnected fluctuation network rather than isolated particles. Although this behavior resembles spinodal amplification of concentration fluctuations, it differs fundamentally from classical thermodynamic spinodal decomposition. In particular, the fluctuations do not evolve through continuous self-similar coarsening. Instead, the fluctuation-dominated state collapses abruptly at $t \approx 53$ s: $S(0)$ decreases sharply from ~ 11 to ~ 0.5, the intermediate-q feature disappears, and the scattering profile becomes consistent with weakly interacting crystalline particles. Simultaneously, the characteristic particle size increases rapidly from ~ 120 to ~ 400 nm, indicating rapid crystallization-driven restructuring of the ACC network through a dissolution–reprecipitation process.

In stage IV, $S(q)$ no longer exhibits any structural feature and instead evolves smoothly toward unity over the full q range, indicating a weakly correlated and nearly ideal particle dispersion with strongly reduced compressibility. The disappearance of both the low-q enhancement and the intermediate-q correlations confirms the loss of the fluctuation network and the absence of residual mesoscopic organization.

Overall, the data reveal a transient fluctuation-amplified metastable state that is rapidly terminated by crystallization-driven restructuring rather than by classical spinodal coarsening.

S.I. 4: Combined pH, Q_P, SAXS and WAXS representation

The combined analysis of the Q_P evolution, pH measurements, SAXS, and WAXS data provides a comprehensive view of the structural evolution of the system under stirring at 250 rpm. Distinct dynamical regimes are identified through the time dependence of Q_P, as shown in Fig. 1.S4. The 2D-WAXS data are reported at 0.5 s time intervals in order to capture the rapid structural changes occurring during the transformation process.

A more accurate representation is shown in Fig. 2.S4, where both the intensity

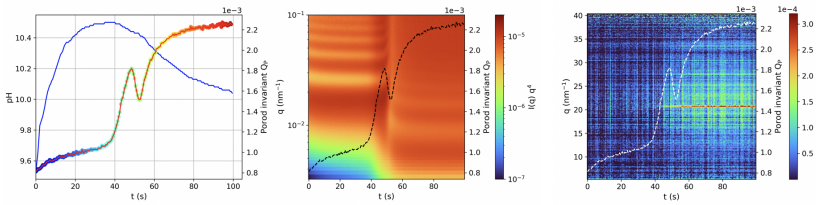

Figure 1.S4: Combined plots showing the time evolution of the different parameters governing the precipitation of the $CaCO_3$ particles. From left to right: pH and Q_P, 2D Porod plot of $I(q)q^4$ with Q_P superimposed and 2D-WAXS data sets measured every 0.5s combined with the evolution of Q_P

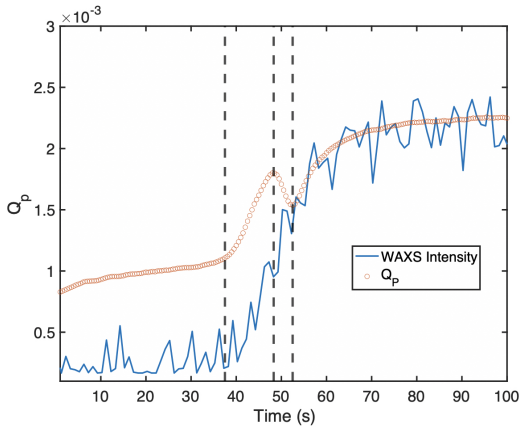

Figure 2.S4: 1D-WAXS data sets measured every 1s combined with the evolution of Q_P

and Q_P are additionally binned into 1 s intervals, clearly demonstrating that crystallization occurs during stage II.

Weak calcite reflections become detectable already during stage II in the WAXS signal and progressively increase throughout stages III and IV, indicating the nucleation and subsequent growth of crystalline calcite domains (see Fig. 2.S4). Importantly, the WAXS analysis remains particularly challenging because the crystalline contribution is extremely weak compared to the scattering from water. The water peak dominates the total scattering intensity by approximately five orders of magnitude, and the WAXS patterns presented here are obtained only after subtraction of this dominant water contribution. As a consequence, the resulting WAXS data remain intrinsically noisy, making the extraction and interpretation of the ACC WAXS data and crystalline signal delicate.

From these observations, the onset of crystallization is identified in the middle of stage II, where the increase in Q_P exhibits a faint kink while the ACC fringes

begin to shift toward higher q. This trend becomes amplified in stage III, where a pronounced dip in Q_P is observed together with a progressive loss of definition of the interference fringes in the SAXS form factor $P(q)$. This behavior indicates a gradual loss of well-defined particle integrity and a reduction of coherent particle-scale scattering, consistent with the structural destabilization of the primary objects.

Notably, the onset of crystallization is also positively correlated with the decrease in pH during stage II, followed by a transient plateau in stage III. From a chemical perspective, this suggests that crystallization is accompanied by the consumption of Ca^{2+} and CO_3^{2-} ions, whereas the ACC destabilization occurring in stage III proceeds at nearly constant pH and Ca^{2+} activity (see Supplementary Section S5).

Therefore, the appearance and progressive reinforcement of calcite Bragg reflections correlate temporally with the regime where Q_P starts to increase during stage II and continues into stage III, where Q_P subsequently reaches a minimum.

Overall, the combined SAXS/WAXS, pH and Q_P analysis reveals a multiscale transformation pathway in which particle-level structural integrity progressively decreases while crystalline order gradually emerges. The intermediate regime, spanning the end of stage II and stage III, corresponds to a transient state characterized by weakened particle correlations, enhanced fluctuations, and the onset of calcite nucleation, ultimately leading to the predominantly crystalline state observed in stage IV.

S.I. 5: Precipitation Experiments and Solution Speciation

In order to gain further insight into solution speciation during precipitation, the pH and Ca^{2+} activity, $a_{Ca^{2+}}$, were measured. It should be noted that these experiments were performed independently from the ESRF measurements and under slightly different experimental conditions. In particular, Ca^{2+} activity measurements required the addition of KCl to maintain constant ionic strength, and both the stirring configuration and the experimental setup within the beaker differed from those used in the in situ experiments. These differences necessarily affect the absolute kinetics and associated time scales. Nevertheless, despite these variations, the measurements provide a consistent description of the precipitation process. In particular, they reproduce the same sequence of four well-defined stages, indicating that the underlying mechanistic evolution is robust with respect to experimental conditions.

Calibration of the pH Probe

The pH electrode was conditioned by immersion in 1.0 M HCl for 15 min prior to each experiment. Following conditioning, the electrode was calibrated using a three-point calibration with standard buffer solutions at pH 7, 10, and 11.

Calibration of the Calcium Ion-Selective Electrode (Ca-ISE)

The Ca-ISE probe was calibrated prior to the experiments to enable in situ determination of Ca^{2+} activity. To maintain constant ionic strength, both the calcium solution and the blank solution were prepared in a 50 mM KCl background. Calibration was performed by continuous addition of a calcium solution (20 mM $CaCl_2$ and 50 mM KCl) into 50 mL of a 50 mM KCl blank solution using a Titrando autotitrator system. The calcium solution was added at a constant rate of 2.5 mL min^{-1}, while potentiometric signals (mV) were recorded every 10 s.

Thermodynamic calculations of calcium activity were performed at 1 min intervals by simulating the continuous addition process, using recorded ambient temperatures and the Visual MINTEQ software. The Davies equation was employed with a parameter $b = 0.3$.

Calibration curves were constructed by plotting the measured potentials (mV) against the logarithm of the calculated calcium ion activity, in accordance with the Nernst equation:

$$E = E_0 + \frac{RT}{zF} \ln a_{Ca^{2+}}, \tag{18}$$

where E is the measured potential, E_0 is the standard electrode potential, R is the gas constant, T is the temperature, z is the ionic charge, F is Faraday's constant, and $a_{Ca^{2+}}$ is the calcium ion activity.

Precipitation Experiments

For spontaneous precipitation experiments, a 50 mL solution containing 9 mM $CaCl_2{\cdot}H_2O$ and 50 mM KCl was prepared and transferred into a 150 mL beaker (8 cm diameter). The solution was continuously stirred at 500 rpm using a 2 cm magnetic stirrer bar. The pH electrode and calcium ion-selective electrode (Ca-ISE) were immersed in the solution, and potentiometric measurements were recorded at intervals of 2 s for pH and 5 s for Ca-ISE.

Subsequently, 50 mL of a 9 mM Na_2CO_3 solution was added using an automatic titrator at a rate of 375 mL min^{-1} (8 s total addition time). The reaction was allowed to proceed until complete precipitation and the establishment of a stable pH plateau, typically after $\sim$700 s.

The collected precipitates were washed with deionized water and ethanol, and dried for subsequent characterization by powder XRD and SEM.

Monitoring of Turbidity Changes in Solution

Turbidity dynamics were recorded as digital video files (MP4 format) using a fixed-mount camera directed at the sample vessel. All videos were analyzed using a custom Python pipeline built on OpenCV (cv2), NumPy, pandas, and SciPy. The frame rate was obtained directly from the video metadata, and analyses could be initiated from an arbitrary start time to exclude pre-experiment footage.

A rectangular Region of Interest (ROI) enclosing only the liquid-containing area was selected interactively on the first frame of the analyzed segment. The ROI coordinates were stored and applied uniformly to every subsequent frame. To verify the suitability of the selected region, baseline mean pixel intensity was assessed against empirical thresholds prior to analysis.

Each video frame within the selected ROI was converted from BGR color space to 8-bit grayscale. The mean pixel intensity ($\bar{I}$), defined as the arithmetic mean of all pixel grey values within the ROI, was computed for each frame and recorded alongside its absolute video timestamp. It is important to note that mean pixel intensity is not a direct or calibrated measure of turbidity in the classical optical sense (e.g. nephelometry or transmittance). Rather, it reflects the overall optical state of the solution environment as captured by the camera under fixed lighting conditions. In a clear, particle-free solution, $\bar{I}$ remains relatively stable and low, as the liquid is largely transparent and contributes little reflected light to the camera sensor. As solid particles nucleate, grow, and aggregate within the solution, the suspension progressively whitens due to increased back-scattering and diffuse reflection of ambient light from particle surfaces, resulting in a systematic increase in $\bar{I}$ over time. This behavior is consistent with the well-known optical phenomenon whereby dense particle suspensions appear white or opaque because multiple scattering events randomize photon directions, returning a large fraction of incident light toward the observer. This makes $\bar{I}$ a practical and sensitive indirect indicator of evolving optical conditions within the vessel. Even in the absence of absolute turbidity calibration, the temporal profile of $\bar{I}$ provides meaningful qualitative insight into key stages of the process: the induction period preceding particle formation, the onset and rate of densification, and the approach to a steady-state or plateau. Gradual rises, sudden jumps, or inflection points in the $\bar{I}$ signal can each be interpreted as signatures of distinct physical events, such as the onset of nucleation, bulk solidification, or the completion of a phase transition, making this approach well-suited for comparative and kinetic analysis of crystallization or precipitation phenomena.

The raw frame-rate intensity signal was smoothed using a Savitzky–Golay filter to suppress sensor noise while preserving the underlying temporal trend. Two smoothing levels were applied: a short-window filter to retain rapid fluctuations, and a long-window filter to reveal the general turbidity trajectory. Both filters used a third-order polynomial fit.

Thermodynamic Calculations of Solution Speciation

Solution speciation calculations were performed using Visual MINTEQ (Minteq v4 database), considering only simple ion pairing and neglecting higher-order complexes and solid-phase formation. The results are summarized in Table 1.

The calcium ion activity in the initial solution and after full mixing with carbonate is given by:

$$a_{\mathrm{Ca}^{2+}}^{\mathrm{initial}} = 3.43 \text{ mM} \tag{19}$$

$$a_{Ca^{2+}}^{mixed} = 1.23 \text{ mM} \tag{20}$$

The calculated pH of the fully mixed solution is:

$$pH_{calc} = 10.73 \tag{21}$$

Experimental measurements yield slightly lower values:

$$a_{Ca^{2+}}^{exp} = 1.03 \pm 0.07 \text{ mM} \tag{22}$$

$$pH_{exp} = 10.50 \pm 0.01 \tag{23}$$

The discrepancy between calculated and experimental values suggests the formation of metastable complexes in solution.

Table 1: Summary of calculated and experimental solution speciation and pH values.

Parameter	Calculated	Experimental
Ca^{2+} activity (mM)	1.23	1.03 ± 0.07
pH	10.73	10.50 ± 0.01

Precipitation pathway

The precipitation reactions, monitored through in-situ measurements of pH and calcium activity, followed the same four-stage pathway (Figure S5). During Stage I, the addition of the carbonate precursor resulted in an increase in pH accompanied by a decrease in calcium activity due to dilution and ion clustering. Immediately upon completion of mixing, the solution became turbid, as reflected by the increase in mean pixel intensity, after which both pH and calcium activity stabilized. The experimentally observed pH and calcium activity values during this stage were lower than the corresponding equilibrium-based theoretical predictions, consistent with the rapid formation of amorphous calcium carbonate (ACC). During Stage I, ACC persists in the reaction medium as a metastable phase, maintaining a dynamic equilibrium with the solution.

Following this initial metastable state, both pH and calcium activity exhibited a small decrease (Stage II). The further consumption of calcium ions and pH decrease indicate the onset of phase transformation processes, which can be correlated with ACC maturation and the emergence of crystalline phases, accompanied by a continuing increase in turbidity. In Stage III, both pH and calcium activity signals stabilized again for a short period. This plateau region represents a transient steady-state, where the nucleation and growth of crystalline phases progressively drive the solution toward undersaturation with respect to ACC, thereby promoting its dissolution and continuous supply of ions for the crystalline phases. The decreasing mean pixel intensity observed in Stage III

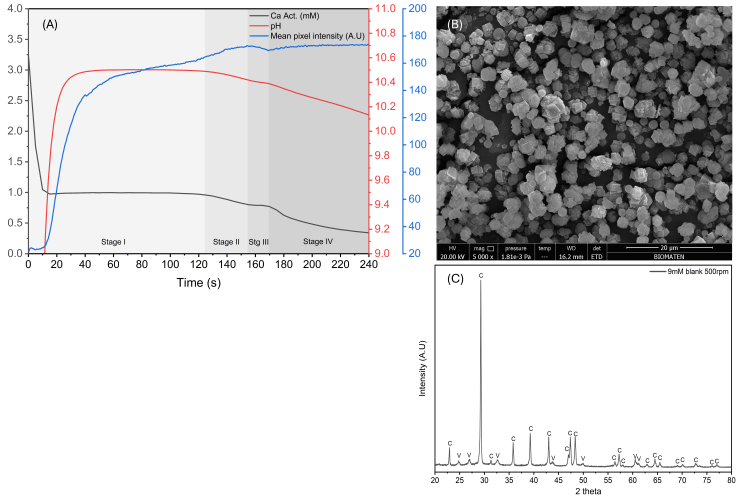

Figure 1.S5: (A) Time resolved monitoring of pH, calcium ion activity and mean pixel intensity, the addition of carbonate solution starts at t= 0 s; (B) SEM image and (C) powder XRD of the final product.

correlates with loss of ACC volume and is consistent with the drop in Porod invariant observed in SAXS measurements. Stage IV corresponds to a second and more pronounced drop in both pH and calcium activity signals, associated with a further consumption of supersaturation by the crystalline phases.

S.I. 6:Experimental set up

The experimental setup is shown in Fig. 1.S6. A movie illustrating the setup and its operation is provided as supplementary material. It highlights the sudden onset of turbidity at the end of Stage I. The (Na_2CO_3) solution is dispensed automatically inside the beaker containing the ($CaCl_2$) solution, a magnetic stir bar, and a pH electrode, which records the pH in real time.

References

[1] A. Gibaud, SAXS-analysis a user friendly program to analyze SAXS data, (2026).

[2] L. Khurts, H. Shaked, J. Sklar, E. Prudnikov, S. Prévost, G. Manna, M. Sztucki, A. Katsman, and B. Pokroy, Proc. Natl. Acad. Sci. USA **122**, e2421961122 (2025).

[3] J. K. Percus and G. J. Yevick, Phys. Rev. **110**, 1 (1958).

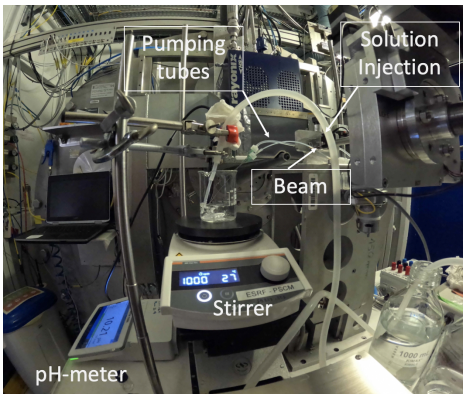

Figure 1.S6: Experimental setup showing the different devices used during the experiment. The (Na_2CO_3) solution is pumped from the 1000 mL bottle located at the bottom right of the figure using an automatic Vevor dispenser. The stirring speed is set prior to the experiment. The pH is automatically recorded for each captured frame.

[4] J. S. Pedersen, Adv. Colloid Interface Sci. **70**, 171–210 (1997).

[5] J. Teixeira, J. Appl. Crystallogr. **21**, 781–785 (1988).

[6] L. S. Ornstein and F. Zernike, Proc. R. Acad. Sci. Amsterdam **17**, 793–806 (1914).